Photofragment slice imaging studies of pyrrole and the Xe···pyrrole cluster

L. Rubio-Lago, D. Zaouris, Y. Sakellariou, D. Sofikitis, T. N. Kitsopoulos, F. Wang, X. Yang, B. Cronin, A. L. Devine, G. A. King, M. G. D. Nix, M. N. R. Ashfold, and S. S. Xantheas

Articles you may be interested in

A combined spectroscopic and theoretical study of propofol·(H2O)3
J. Chem. Phys. **137**, 074303 (2012); 10.1063/1.4743960

Isotope dependent, temperature regulated, energy repartitioning in a low-barrier, short-strong hydrogen bonded cluster
J. Chem. Phys. **132**, 244301 (2010); 10.1063/1.3430525

A theoretical and experimental study of the ethyl-p-aminobenzoate (H 2 O) n (n=1–4) complexes
J. Chem. Phys. **113**, 8531 (2000); 10.1063/1.1318196

Photodissociation of CH stretch overtone excited CH 3 Cl and CHD 2 Cl (ν CH =5): Cl spin–orbit branching and atomic fragment yields
J. Chem. Phys. **109**, 7810 (1998); 10.1063/1.477427

Electronic spectroscopy and dynamics of the monomer and Ar n clusters of 9-phenylfluorene
J. Chem. Phys. **109**, 7113 (1998); 10.1063/1.477395

Photofragment slice imaging studies of pyrrole and the Xe···pyrrole cluster

L. Rubio-Lago, D. Zaouris, Y. Sakellariou, D. Sofikitis,[a] and T. N. Kitsopoulos[b]
Institute of Electronic Structure and Laser, Foundation for Research and Technology-Hellas, 71110 Heraklion, Crete, Greece and Department of Chemistry, University of Crete, 71110 Heraklion, Crete, Greece

F. Wang[c] and X. Yang
State Key Laboratory for Molecular Reaction Dynamics, Dalian, 116023 Liaoning, People's Republic of China

B. Cronin, A. L. Devine, G. A. King, M. G. D. Nix, and M. N. R. Ashfold
School of Chemistry, University of Bristol, Bristol BS8 1TS, United Kingdom

S. S. Xantheas[b]
Chemical and Materials Sciences Division, Pacific Northwest National Laboratory, 902 Battelle Boulevard, P.O. Box 999, MS K1-83, Richland, Washington 99352

The photolysis of pyrrole has been studied in a molecular beam at wavelengths of 250, 240, and 193.3 nm, using two different carrier gases, He and Xe. A broad bimodal distribution of H-atom fragment velocities has been observed at all wavelengths. Near threshold at both 240 and 250 nm, sharp features have been observed in the fast part of the H-atom distribution. Under appropriate molecular beam conditions, the entire H-atom loss signal from the photolysis of pyrrole at both 240 and 250 nm (including the sharp features) disappear when using Xe as opposed to He as the carrier gas. We attribute this phenomenon to cluster formation between Xe and pyrrole, and this assumption is supported by the observation of resonance enhanced multiphoton ionization spectra for the (Xe···pyrrole) cluster followed by photofragmentation of the nascent cation cluster. *Ab initio* calculations are presented for the ground states of the neutral and cationic (Xe···pyrrole) clusters as a means of understanding their structural and energetic properties. © *2007 American Institute of Physics.* [DOI: 10.1063/1.2754688]

I. INTRODUCTION

A prototypical six π-electron heteroatomic aromatic molecule like pyrrole (C_4H_5N) constitutes an ideal model for the study of more complex systems, such as nucleobases and aromatic aminoacids.[1–4] Furthermore, pyrrole, along with other nitrogen containing heterocyclic compounds, is an important source of nitrogen fuel in coal[5] and heavy oils as well as an important component in many oil-based products. Pyrrole and related molecules also play an important role in the synthesis of biologically active compounds, pesticides, polymers, and organometallic complexes.[6]

The UV absorption spectra of pyrrole is broad and unstructured, presenting two intense absorption bands around 165 and 210 nm and a weaker feature around 240 nm.[7,8] The interaction of the $^1\pi\pi^*$ *bright* states and $^1\pi\sigma^*$ *dark* states and its effects on the photochemistry of pyrrole or similar heteroaromatic molecules, and even in DNA bases, have been reported. H-atom elimination is the main fragmentation channel upon excitation of pyrrole at longer UV wavelengths. The $S_1(^1A_2, {}^1\pi\sigma^*)$ state of pyrrole presents a 3s Rydberg character for short N–H bond distances but becomes antibonding when the separation increases (Fig. 1).[2,4,9–11] Direct absorption from the $S_0(X\,^1A_1)$ ground state to the excited

$^1\pi\sigma^*$ state of $^1A_2$ electronic symmetry is electric dipole forbidden, but vibrational coupling with the nearby excited states of $^1A_1$, $^1B_1$, and $^1B_2$ symmetries [particularly the bound $^1B_2$ state due to the dominant oscillator strength of the $^1B_2 \leftarrow X\,^1A_1(\pi^* \leftarrow \pi)$ transition] increases the vibronic transition probability. The relative positions (in energy space) of the $^1\pi\pi^*$ and the $^1\pi\sigma^*$ potential energy surfaces (PESs) determines the dissociation dynamics. In the case of pyrrole, the $^1\pi\sigma^*$ PES is located below the $^1\pi\pi^*$ PES, facilitating a rapid internal conversion (IC) from the $^1\pi\pi^*$ to the $^1\pi\sigma^*$ state. Much of the photochemistry of the $^1\pi\pi^*$ state is thus determined by the dynamics of the $^1\pi\sigma^*$ PES. A conical intersection between S_0 and S_1 could facilitate internal conversion from the excited state towards the ground state. The behavior of the $^1\pi\sigma^*$ state can be directly attributed to the following two properties related to its electronic structure: First, the antibonding σ^* orbital is localized on the N–H bond, which makes H-atom loss via the $^1\pi\sigma^*$ state a highly probable dissociation channel. Second, the conical intersection of the $^1\pi\sigma^*$ with the ground state is a result of the fact that the ground ($X\,^1A_1$) state of pyrrole does not correlate with the ground ($X\,^2A_2$) state of the pyrrolyl (C_4H_4N) fragment. Instead, it correlates asymptotically with H ($1s$) and the $^2A_1$ excited state of pyrrolyl. The excited ($1\,^1A_2$) state of pyrrole correlates with H ($1s$) and the ground state of pyrrolyl (see Fig. 1).

The photodissociation dynamics of pyrrole has attracted

[a] Also at Department of Physics, University of Crete.
[b] Authors to whom correspondence should be addressed.
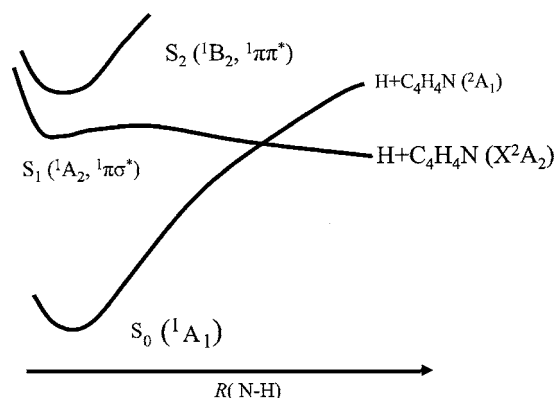[c] Also at IESL-FORTH.

FIG. 1. Cuts through schematic potential energy curves for the ground and excited states of pyrrole, showing the asymptotic correlations for H-atom loss.
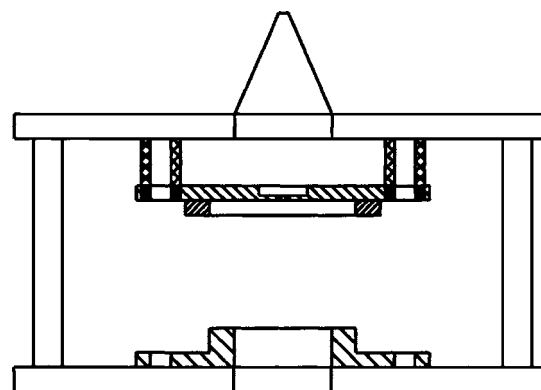

FIG. 2. A schematic diagram of the ion optics used in the present experiment. As noted in the text the supporting grounded rods are moved to a larger diameter than in the original design described in Ref. 17.

significant attention in the past few years.[2,4,12–15] In the work of Temps and co-workers the H-atom elimination channel has been studied by velocity map imaging, showing a bimodal kinetic energy distribution. The *fast* H atoms are produced upon excitation of the first excited state of pyrrole $(1\ ^1A_2)$, followed by a prompt dissociation of the N–H bond, giving rise to an intense, narrow peaked kinetic energy distribution. The *slow* H atoms originate from the dissociation of ground $(X\ ^1A_1)$ state molecules after IC from the excited state, producing a broad signal at low kinetic energies. A mean recoil anisotropy parameter of $\beta = -0.37 \pm 0.05$ is obtained for the fast atoms, whereas the slow H-atom distribution was found to be nearly isotropic. More recently, in the experiments of Ashfold and co-workers, the high velocity resolution attainable in the Rydberg tagging method allowed the observation of the vibrational structure of the pyrrolyl coproduct. Analysis of the fragment modes, which are evident in the kinetic energy release (KER) spectrum, suggests that the $1\ ^1A_2 \leftarrow X\ ^1A_1$ transition is *selectively* induced by the excitation of one or more quanta of vibration in certain nonsymmetric skeletal modes of the parent molecule. The measured angular distribution of the H atoms was shown to depend on the identity of the vibrational state of the pyrrolyl cofragment—consistent with the view that the parent mode providing vibronic enhancement to the $1\ ^1A_2 \leftarrow X\ ^1A_1$ excitation maps through into the product. Although most of the peaks appearing in the KER spectrum show a negative anisotropy, there are obvious exceptions, reaching values as high as $\beta \sim +1$.

In this work we use the slice imaging technique coupled with a vacuum ultraviolet (UV) $(1+1')$ REMPI scheme to detect H atoms from the photodissociation of pyrrole. The experiments were carried out at 193, 240, and 250 nm using different carrier gases. In contrast to the 243 nm based $(2+1)$ REMPI scheme used by Temps *et al.*, the vacuum ultraviolet (VUV) approach has a much higher resolution, thus allowing the observation of much of the vibrational structure reported by Cronin *et al.* Effects of the carrier gas on the measured H-atom signal are also presented, which strongly support the formation of mixed clusters of Xe with pyrrole molecules with entirely different photolysis behavior—especially in the long wavelength region. In

Sec. II we outline the experimental and computational details of our study. In Sec. III we present the experimental results for the photolysis of pyrrole at the three different wavelengths as well as the REMPI photofragment and photoelectron spectra associated with the (Xe···pyrrole) dimer cluster. These results are discussed in Sec. IV together with theoretical results for the (Xe···pyrrole) cluster. Final conclusions and future plans are presented in Sec. V.

II. EXPERIMENTAL AND THEORETICAL METHODS

A. Experiment

The slice imaging experiments presented here were performed in a recently enhanced apparatus, but all features and procedures relevant to the present study have been described previously.[16] In the present experiment we use a new set of ion optics to perform slicing and velocity mapping using a single field.[17] In the original design, four grounded rods were used as standoffs to hold the repeller and extractor at the proper distances. These rods were located on a diameter of 50 nm with respect to the time of flight axis. However, we noticed that for long delays (>300 ns) the rods started to affect the roundness of the images. Hence it was necessary to move the rods to a larger radius (96 mm). The repeller is held using flush screws while the extractor is bolted onto a larger grounded plate as shown in Fig. 2. In order to maintain space focusing, the separation between repeller and extractor was increased slightly from 22.5 mm reported previously to 31.5 mm.

Photolysis UV radiation at 240 and 250 nm is generated by Nd:yttrium aluminum garnet (Spectra Physics Pro Series 450) pumping a master oscillator power oscillator system (Spectra Physics 730D10). The 193 nm laser light is generated from a compact excimer laser (Neweks PSX-501) and is polarized using Brewster reflection.

We use a VUV-UV $(1+1')$ REMPI scheme for detecting the H atoms. The VUV radiation at 121.6 nm pumps the hydrogen atom to its $2p$ state, from where it is ionized by the UV light at 364.7 nm. The VUV laser radiation is generated using nonresonant tripling by focusing the 364.7 nm radiation produced by an excimer pumped dye laser system (LPX 400, FL3002) with a 150 mm focal length lens in a cell

containing 170 mbar Kr and 370 mbars of Ar. The resultant VUV beam is focused onto the 2 mm diameter molecular beam using a MgF_2 lens (Crystran) while the residual 364.7 nm laser light is focused about 1.5 cm behind the beam. Both UV and VUV laser beams remain mutually very well collimated. Optimization of both the alignment of the VUV and UV laser beams and the Kr/Ar mix ratio in the tripling cell is performed by monitoring the H atoms produced by running a current of 3 A through a tungsten filament. The red-hot filament generates H atoms from the pyrolysis of background pump oil (the base pressure in the detector region is 1×10^{-7} mbar). When the hot filament is turned off, negligible amounts of H atoms are observed.

Due to the high velocity of the H-atom photofragments, the laser bandwidth used to excite the $2p \leftarrow 1s$ transition is narrower than the Doppler profile. In order to record all the velocities with similar probabilities, the VUV laser is scanned over the Doppler profile of the $2p \leftarrow 1s$ transition during the experiments. The phase matching conditions in the tripling cell are sufficient to cover the region scanned.

Slice images are obtained using a 300 ns extraction delay and an effective 10 ns detector gate. The repeller voltage used is 1500 V, and the detector voltages are 4.8 kV between back (output) microchannel plate (MCP) and phosphor screen, 1200 V on the back (output) MCP, and pulsing -700 V on the front (input) MCP. Images are obtained using two laser polarization geometries: X (pump), Z (probe), and ZZ geometries, where X is perpendicular to the laser propagation axis (Y) and Z is parallel to the molecular beam. Angular distributions determined from the XZ images are normalized by the angular distributions measured in the corresponding ZZ images thus removing any systematic errors such as detector inhomogeneities.

The molecular beam is produced by a home built pulsed nozzle based on a piezoelectric disk actuator.[18] Pyrrole is freeze thawed and subsequently heated to assist evaporation into the gas line supplying the nozzle. Carrier gas is added to the supply line at a total backing pressure of approximately 500 mbars. The nozzle orifice is 1 mm in diameter and gas pulses of less than 300 μs duration are generated.

B. Theory

Geometry optimizations and subsequent harmonic vibrational analysis for the ground states of pyrrole (C_4H_5N), pyrrole cation ($C_4H_5N^+$), and their complexes with Xe [$(Xe\cdots C_4H_5N)$ and $(Xe\cdots C_4H_5N^+)$] were carried out at the second order Møller-Plesset perturbation (MP2) level of theory.[19] The geometries of all species were optimized using the augmented correlation-consistent basis sets[20] of double (aug-cc-pVDZ) and triple (aug-cc-pVTZ) zeta quality on the C, N, H atoms and the corresponding aug-cc-pVDZ-PP and aug-cc-pVTZ-PP basis sets based on small-core relativistic pseudopotentials[21] for Xe. Harmonic vibrational frequencies were obtained using the combination of double zeta quality basis sets (aug-cc-pVDZ/aug-cc-pVDZ-PP) for all species. In order to converge the energies at the MP2 level of theory we have also performed single point energy calculations with the combination of basis sets of quadruple zeta quality (aug-

cc-pVQZ/aug-cc-pVQZ-PP) at the optimal geometries obtained with the combination of triple zeta sets. All electronic structure calculations were carried out with the GAUSSIAN 03 (Ref. 22) program suite.

III. RESULTS

A. Photolysis at 250 nm

Figure 3(a) shows the XZ image for the photolysis of pyrrole at 250 nm, seeded in He (all images shown are quadrant symmetrized). Figure 3(b) shows the KER spectrum of the H atoms obtained from the image in Fig. 3(a) when using for calibration the value of $D_0(N-H) = 32\,850$ cm^{-1} as determined by Cronin et al. In the KER spectrum of Fig. 3(b) we observe a number of peaks. For comparison purposes we have overlaid our KER spectrum with the one of Cronin et al. obtained at the same wavelength by Rydberg tagging. The agreement between the two experimental spectra is excellent. Aside from the superior velocity resolution of the Rydberg tagging method, the same sharp features (peaks) are observed in the slice imaging data. Our images indicate that a non-negligible yield of H atoms is formed with a small kinetic energy as part of a broad distribution that tails off around 10 000 cm^{-1}. Angular distributions for several of the sharp peaks are shown in Fig. 4. Angular distributions are fitted to the functional form $1 + \beta[P_2 \cos(\theta)]$, where θ is the angle between the photolysis laser polarization (in this case
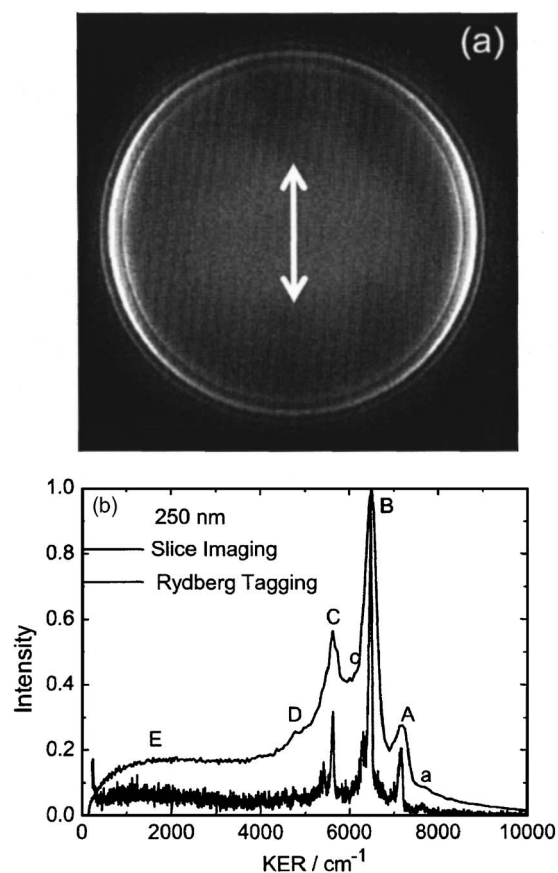

FIG. 3. (a) H-atom photofragment slice image following the photolysis of pyrrole at 250 nm with ε_{phot} aligned vertically. (b) H-atom kinetic energy distribution obtained from image (a) and from Ref. 14.
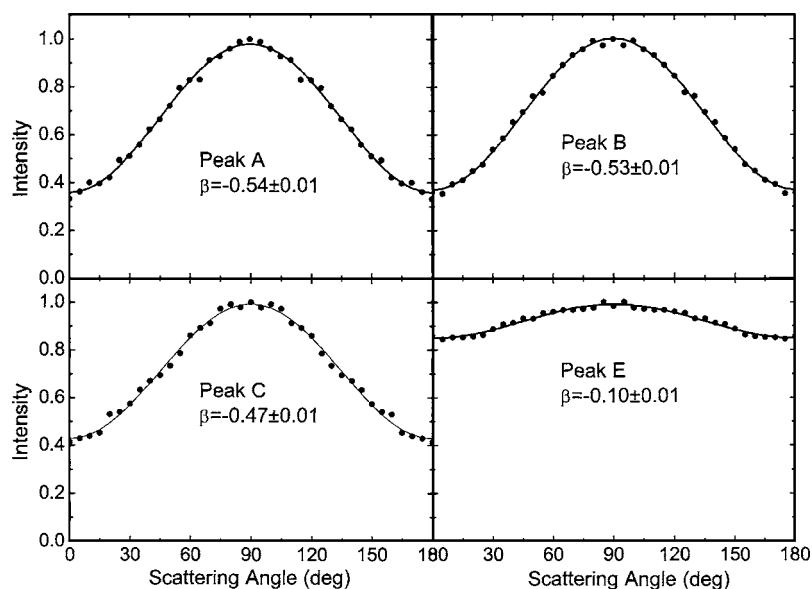
FIG. 4. H-atom photofragment angular distributions for the various peaks in the KER spectrum of Fig. 3(b).

vertical) and the recoil axis and β is the anisotropy parameter. We observe negative values of β that tend towards zero (i.e., an isotropic recoil distribution) as the H-atom velocity becomes small.

When seeding pyrrole in Xe or Kr and expanding under the same conditions of backing pressure, pulse duration, etc., essentially no H-atom release was observed when exciting at 250 nm, and we were unable to obtain an image of reasonable quality.

B. Photolysis at 240 nm

The *XZ* image for the photolysis of pyrrole seeded in He at 240 nm is shown in Fig. 5(a). Figure 5(b) displays the KER spectrum of the H atoms obtained from the image in Fig. 5(a) using the same calibration as in Fig. 3(b). For comparison purposes we have again overlaid our KER spectrum with that recorded at the same wavelength by Cronin *et al.* The agreement between the two experimental spectra is once again excellent. Most of the sharp features observed in the very high resolution Rydberg tagging experiment are resolved or partially resolved in the slice imaging data. Angular distributions for several of the peaks are shown in Fig. 6. As in the case of 250 nm and in addition to the sharp features at large H-atom KER, we observe an underlying broad distribution in the slice imaging data that tail off at $\sim 11\,000$ cm^{-1}.

When seeding pyrrole in Xe or Kr and expanding under the same conditions of backing pressure, pulse duration, etc., essentially no H-atom release was observed when exciting at 240 nm, and we were unable to obtain an image of reasonable quality.

C. Photolysis at 193 nm

Figure 7(a) shows the *XZ* image for the photolysis of pyrrole at 193 nm when seeding in He, whereas the KER spectra when seeding in both He and Xe are shown in Fig. 7(b). Unlike the longer excitation wavelength behavior reported above, the photolysis of pyrrole at 193 nm using Xe

as the carrier gas appears to be just as efficient as when using He. The main difference with the spectra obtained at the two longer wavelengths is the absence of any sharp features in the KER spectra. A bimodal distribution is observed and the H atoms appear to recoil with very low anisotropy. When comparing to the previous Rydberg tagging experiments, the
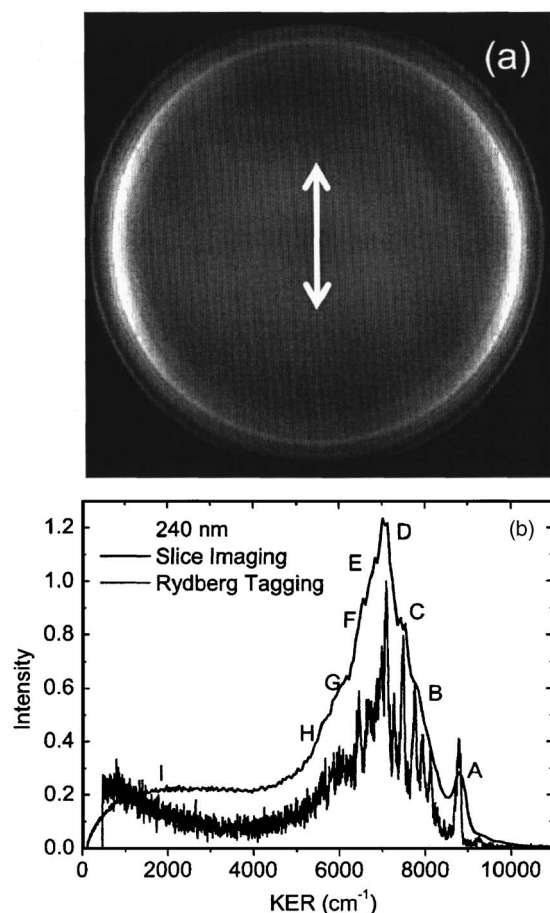

FIG. 5. (a) H-atom photofragment slice image following the photolysis of pyrrole at 240 nm with $\varepsilon_{\text{phot}}$ aligned vertically. (b) H-atom kinetic energy distribution obtained from image (a) and from Ref. 14.
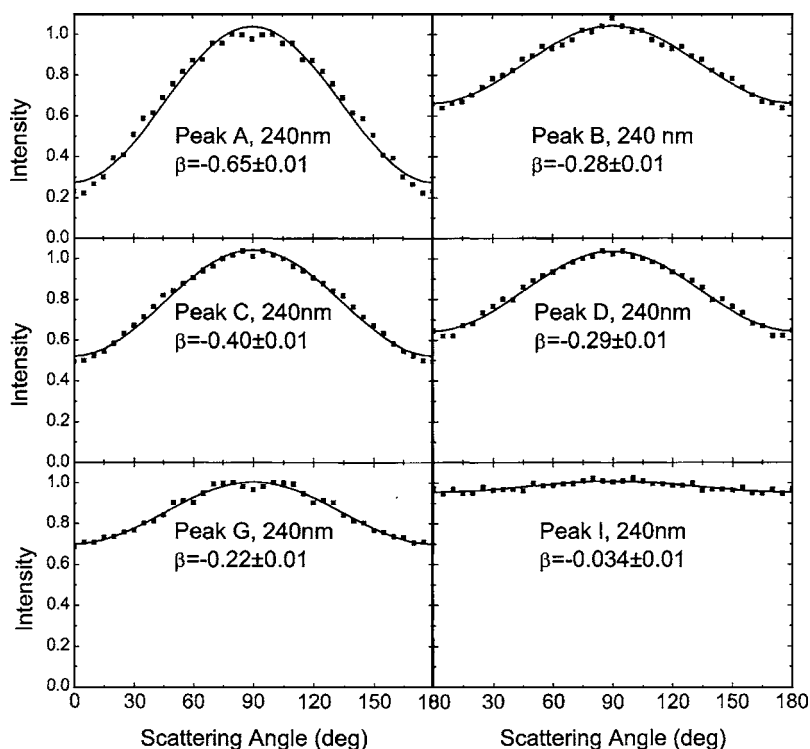
FIG. 6. H-atom photofragment angular distributions for the various peaks in the KER spectrum of Fig. 5(b).

main difference of our data is the relative intensity of the fast and slow features in the KER distributions.[13,14] Only a slight difference between the intensities of the peaks corresponding to the fast and slow H atoms is observed among the two sets of data obtained when using He and Xe as carrier gases. From the angular distributions shown in Fig. 8, once again we see that the anisotropy parameter approaches zero as the velocity of the H atoms is reduced.

D. REMPI photofragment and photoelectron spectra

When using Xe as the seeding gas in the molecular beam, several $(1+1')$ REMPI transitions are observed: λ =363.898, 363.844, and 363.796 nm. Excitation at these wavelengths produces Xe^+ ions in the mass spectrum, and a typical photofragment image of these Xe^+ products is shown in Fig. 9(a). A series of rings are observed with low anisotropy. At larger radii a strongly anisotropic feature is present as shown in Fig. 9(b). This is the same image as that shown in Fig. 9(a) but with enhanced contrast. The appearance of the images is the same for all the resonances observed in this region and only the yield of Xe^+ varies between the resonances. The Xe^+ KER spectrum obtained from the photofragment image is shown in Fig. 10(a).

The REMPI photoelectron spectrum obtained following excitation at λ=363.898 nm was also recorded and results are shown in Fig. 10(b). Three main peaks are observed along with two satellite features. The spectra and the laser wavelength in this region is calibrated by measuring the $(3+1)$ REMPI of atomic Xe via the $5d[5/2]$, $J=3$ state at 82 430 cm^{-1}.

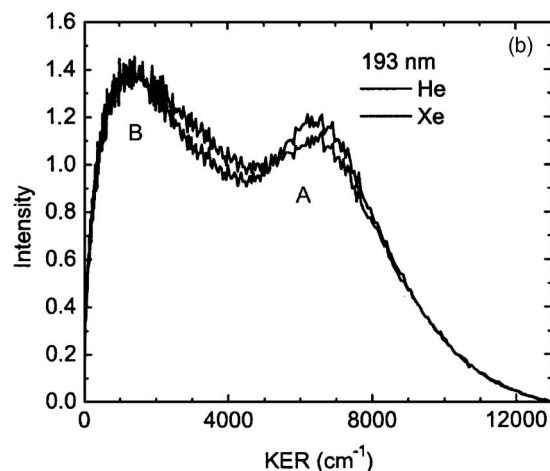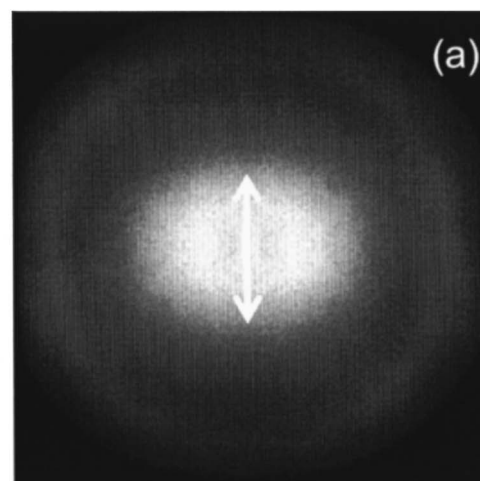
FIG. 7. (a) H-atom photofragment slice image following the photolysis of pyrrole at 193 nm with ε_{phot} aligned vertically. (b) H-atom kinetic energy distribution obtained at 193 nm for Xe and He carrier gases.
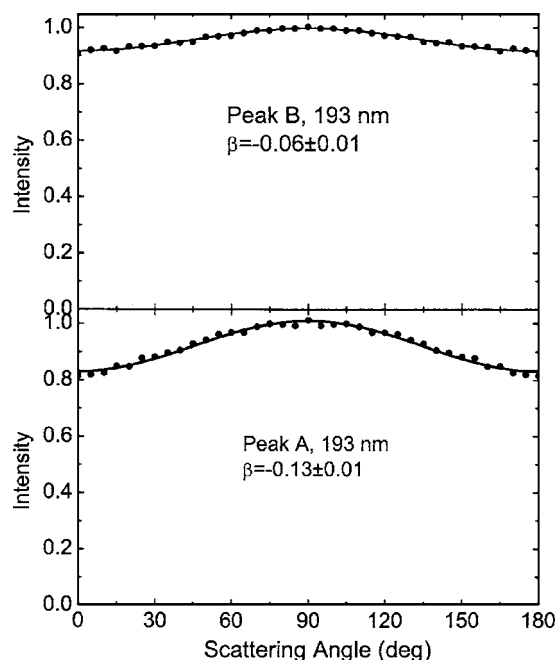
FIG. 8. H-atom photofragment angular distributions for the various peaks in the KER spectrum of Fig. 7(b).

IV. DISCUSSION

A. Photolysis of pyrrole

In the previous studies of pyrrole photodissociation at 243 nm by Temps and co-workers, a bimodal H-atom KER distribution attributable to N–H bond fission was observed. Our results at all three wavelengths also show this characteristic bimodal distribution. The intense fast channel was attributed to "direct" dissociation involving vibronically induced excitation from the S_0 state to the $S_1(^1A_2, ^1\pi\sigma^*)$ state (see Fig. 1). The slow products observed when exciting at short wavelengths are readily attributable to a mechanism that involves initial excitation from the $S_0(^1A_1)$ to the $S_2(^1B_2, ^1\pi\pi^*)$ state, followed by internal conversion back to the S_0 ground state and subsequent unimolecular (statistical) dissociation. At longer wavelengths, however, the photon energies are insufficient to access the $^1B_2$ state. The slow H-atom products observed when exciting pyrrole in He carrier gas at 240 and 250 nm (which are less evident in the Rydberg tagging data) may raise from the dissociation of ground state pyrrole molecules formed by coupling from the $1\,^1A_2$ state at the conical intersection at large R_{N-H} bond
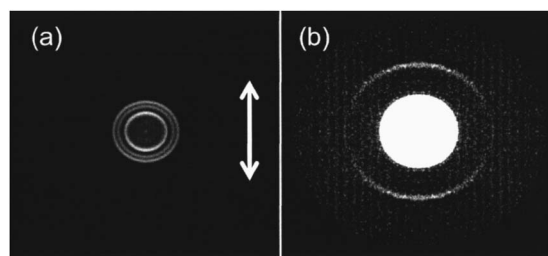

FIG. 9. (a) Xe⁺ photofragment image following the excitation of pyrrole seeded in Xe at $\lambda = 363.9$ nm, with ε_{phot} aligned vertically. (b) Same image as (a) except that the contrast has been enhanced to reveal the weak anisotropic ring at larger radius.

lengths or from the dissociation of some (unintended) cluster component within our beam. Similar conclusions were reached by Ashfold and co-workers following the photolysis of pyrrole in the range of 193.3 nm $< \lambda_{phot} <$ 254 nm. Their experiments suggested a trend in the relative intensity of the fast and slow peaks, namely, that the slow channel gains in intensity as the photolysis wavelength decreases. For wavelengths $>$240 nm, the unsurpassed velocity resolution offered by the Rydberg tagging[23] method allowed them to resolve well defined structure in the fast channel, attributable to the population of *selected* vibrational levels of the ground state of the pyrrolyl radical. Our adaptation of a $(1+1')$, as opposed to the $(2+1)$, REMPI detection scheme for H atoms eliminates the photoelectron-recoil problem of the latter method resulting in high-resolution images[24] and allows resolution of much of the structure observed by Ashfold and co-workers.[14,25]

The KER spectrum obtained at 193 nm shows no resolvable sharp features. Its center of gravity in kinetic energy space is barely shifted from that seen in the long wavelength data. When λ_{phot} is reduced from 240 to 193 nm, therefore, the additional energy provided by the photon is largely retained as vibrational excitation of the pyrrolyl moiety. These observations indicate a remarkable degree of vibrational adiabaticity in the dissociation of pyrrole molecules through their $S_1(^1A_2, \pi\sigma^*)$ state.[14,25]

The measured angular distributions for the fast H atoms at 243 nm in the experiments of Temps and co-workers were shown to be anisotropic, associated with a β parameter of ~-0.3. At those wavelengths where it was possible to resolve product vibrational structure, the Rydberg tagging experiments[14] showed that the recoil anisotropy depended on the vibrational level of the pyrrolyl cofragment but averaged to an overall negative β. Our energy resolution does not allow full delineation of these features in the present slice images, but a negative β value is also found for the fast H atoms measured in the present work, that tends towards zero at lower velocities (Figs. 4, 6, and 8).

B. The (Xe⋅⋅⋅pyrrole) cluster

In the present study, when pyrrole is seeded in Xe or Kr, no H-atom photofragments are observed when exciting near the extreme red end of the parent absorption spectrum. We attribute this blockage (quenching) of the N–H bond fission when seeding in Xe to the formation of clusters and below we discuss our specific observation for the (Xe⋅⋅⋅pyrrole) dimer cluster (to be referred to as Xe–Py from now on).

The optimal structures of the ground states of pyrrole (Py, $X\,^1A_1$ of C_{2v} symmetry), its cation (Py⁺, $X\,^2A_2$ of C_{2v} symmetry), and their minima with Xe, (Xe–Py), and (Xe–Py)⁺, at the MP2 level of theory with the combination of basis sets of triple zeta quality (see Sec. II B) are shown in Fig. 11, where the labeling of the atoms is also denoted. These calculations aim in the characterization of the structural and energetic properties of the respective ground states for the neutral and cation (Xe–Py) cluster and will be used as the starting points in future calculations of their excited state manifold. Complexation of the neutral Py as well as its cat-
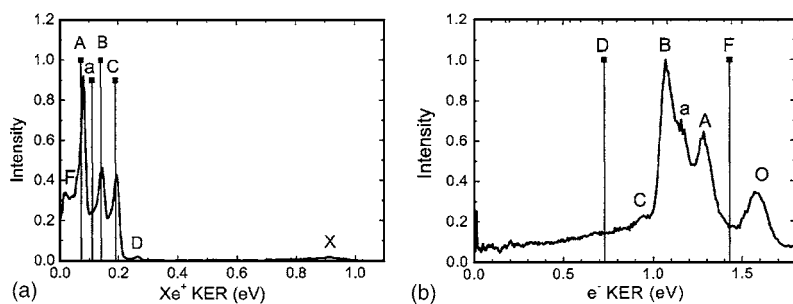
FIG. 10. (a) Xe^+ KER spectrum obtained from the image in Fig. 9. (b) Photoelectron spectrum obtained following the excitation of pyrrole seeded in Xe at $\lambda = 363.9$ nm.

ion $(Py)^+$ with Xe results in two minima, one π bonded with the Xe out of plane (denoted as m_1) the other with the Xe in plane and bonded to hydrogen (denoted as m_2), as shown in Fig. 11. In the case of the (Xe–Py) cluster, both have C_s symmetry (albeit having different planes of symmetry) on the $^1A'$ PES (see Table I). For the $(Xe-Py)^+$ cluster, the π-bonded minimum (m_1) assumes a quasisymmetric geometry (^2A) whereas the hydrogen-bonded minimum (m_2) has C_{2v} symmetry $(^2A_2)$ (for the m_2 structures all atoms lie on the same plane). The (π-bonded) structure of C_s symmetry for $(Xe-Py)^+$ is a first order transition state with an imaginary frequency of 22 cm^{-1}, lying just 0.05 kcal/mol above the local quasisymmetric minimum of C_1 symmetry.

The optimal values of the internal coordinates of all species with the double (first line) and triple (second line) zeta sets are listed in Table I. As expected due to the weak interaction with Xe, the internal coordinates of the (Py) and $(Py)^+$ fragments in both the m_1 and m_2 $(Xe-Py)^+$ minima are minimally perturbed from their isolated gas phase values resulting in slightly distorted, off-C_{2v} geometries. Typical changes due to the weak interaction with Xe are <0.001 Å for the bond lengths involving heavy atoms, <0.0002 Å for the bond lengths involving H [except for the N–H bond length of the H-bonded m_2 minimum of $(Xe-Py)^+$ which changes by 0.006 Å], and <0.05° for the bond angles. The position of Xe with respect to the (Py), $(Py)^+$ fragments is determined

from its distance from the center of mass (M) of the (Py), $(Py)^+$ moieties and the corresponding angle as indicated in Fig. 11 and Table I. The dihedral angle $\delta=[Xe-(M\text{-}N\text{-}H)]$ is uniquely determined ($\delta=90°$ for m_1, $\delta=0°$ for m_2) due to symmetry. It should be noted that the position of (M) is slightly different in the m_1 and m_2 minima due to the slightly different values of the internal coordinates of the (Py) and $(Py)^+$ fragments in the two minima as indicated from the results of Table I. Furthermore for the H-bonded minimum m_2 of the (Xe–Py) cluster the two sets of bond lengths for C_a-C_b, C_a-N, C_a-H_n, etc., and corresponding angles are not exactly identical as the presence of Xe in the plane of the molecule slightly perturbs them but the differences between the two sets are <0.001 Å for the bond lengths and <0.1° for the angles. The $R(Xe\text{-}M)$ distance for the H-bonded minimum (m_2) is ~1.0 Å longer than the one for the π-bonded minimum (m_1).

The corresponding energies (in a.u.) of all species with the combination of basis sets up to quadruple zeta quality are shown in Table II. The harmonic vibrational frequencies at the MP2//aug-cc-pVDZ/aug-cc-pVDZ-PP level of theory are shown in Table III. The corresponding harmonic zero-point energies are 51.84 (Py), 55.15$(Py)^+$, 51.75$(Xe-Py,m_1)$, 51.80$(Xe-Py,m_2)$, 55.54$(Xe-Py^+,m_1)$, and 55.71 kcal/mol $(Xe-Py^+,m_2)$, respectively. For the neutral (Xe–Py) cluster

Py ($^1A_1$, C_{2v})   (Xe-Py) ($^1A'$, C_s); m_1 (Xe-Py) ($^1A'$, C_s); m_2

Py$^+$ ($^2A_2$, C_{2v})   (Xe-Py)$^+$ (^2A, C_s); m_1 (Xe-Py)$^+$ ($^2A_2$, C_{2v}); m_2
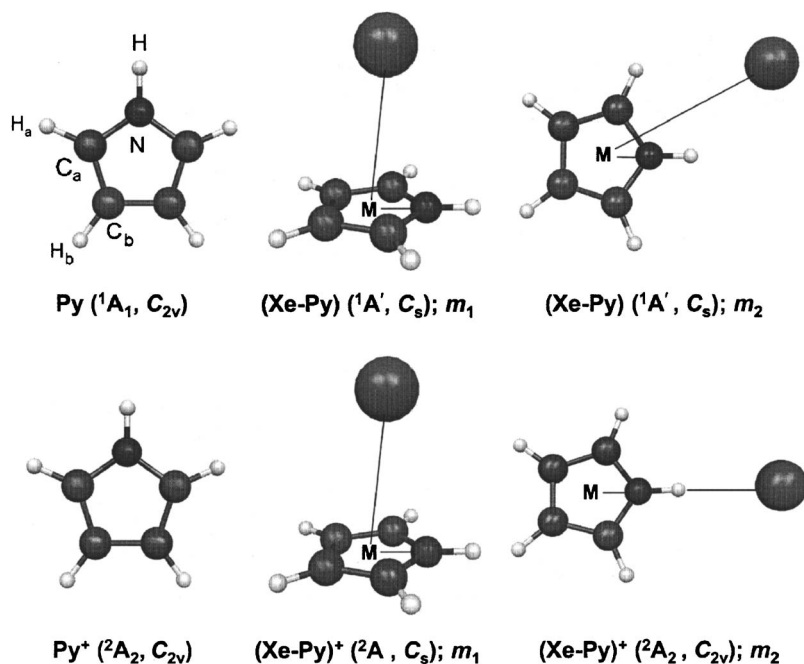
FIG. 11. Optimal geometries for the (Xe–Py) and $(Xe-Py)^+$ clusters.

TABLE I. Optimal geometries for (Py), (Py)$^+$, and their clusters with Xe, (Xe–Py), and (Xe–Py)$^+$ at the MP2 level of theory with the combination of double (first line) and triple zeta (second line) quality basis sets (see text).

Internal coordinates	(Py) $X\,^1A_1\,(C_{2v})$	(Xe–Py)		(Py)$^+$ $X\,^2A_2\,(C_{2v})$	(Xe–Py)$^+$	
		m_1 (π bonded) $^1A'\,(C_s)$	m_2 (H bonded) $^1A'\,(C_s)$		m_1 (π bonded) $^2A\,(C_1)$	m_2 (H bonded) $^2A_2\,(C_{2v})$
R(N–H) (Å)	1.0122	1.0124	1.0122	1.0180	1.0179	1.0235
	1.0051	1.0053	1.0054	1.0114	1.0111	1.0124
R(C$_a$–N) (Å)	1.3795	1.3789	1.3789	1.3656	1.3646	1.3642
	1.3693	1.3687	1.3689	1.3550	1.3541	1.3789
R(C$_a$–H$_a$) (Å)	1.0878	1.0878	1.0878	1.0904	1.0903	1.0904
	1.0761	1.0761	1.0762	1.0788	1.0786	1.0878
R(C$_a$–C$_b$) (Å)	1.3975	1.3980	1.3979	1.4411	1.4407	1.4414
	1.3829	1.3835	1.3835	1.4281	1.4276	1.3980
R(C$_b$–H$_b$) (Å)	1.0890	1.0891	1.0891	1.0891	1.0890	1.0890
	1.0768	1.0769	1.0769	1.0771	1.0770	1.0891
ϕ(H–N–C$_a$) (deg)	124.78	124.75	125.13	125.30	125.28	125.36
	124.87	124.85	125.50	125.39	125.38	124.75
ϕ(H$_a$–C$_a$–N) (deg)	121.30	121.33	121.28	121.62	121.63	121.52
	121.24	121.28	121.27	121.58	121.61	121.33
ϕ(N–C$_a$–C$_b$) (deg)	107.36	107.33	107.37	108.34	108.34	108.48
	107.41	107.39	107.41	108.37	108.39	107.33
ϕ(H$_b$–C$_b$–C$_a$) (deg)	125.50	125.51	125.52	124.91	124.94	125.03
	125.48	125.48	125.49	124.88	124.90	125.51
R(Xe–M) (Å)		3.6117	4.7104		3.7245	4.7964
		3.4978	4.5984		3.5412	4.6960
∂(Xe–M–N) (deg)		84.32	29.09		81.94	0.00
		86.08	27.25		85.09	0.00

the π-bonded minimum (m_1) is lower in energy than the hydrogen-bonded one (m_2) as indicated in Tables III and IV. The order is, however, reversed for the cation (Xe–Py)$^+$ cluster for which the H-bonded minimum (m_2) is lower in energy. The energy separation between the two isomers increases with increasing basis set but it is converged with the combination of the largest basis sets (aug-cc-pVQZ/aug-cc-pVQZ-PP) used in this study. Our best estimate at the MP2 level with the combination of the largest basis sets used in this study (aug-cc-pVQZ/aug-cc-pVQZ-PP) and inclusion of harmonic zero-point energy differences is that for the neutral (Xe–Py) cluster the π-bonded isomer (m_1) is more stable than the hydrogen-bonded isomer (m_2) by $\Delta D_0 = 0.07$ eV, whereas for the cation (Xe–Py)$^+$ the situation is reversed

with the H-bonded minimum being more stable than the π-bonded one by 0.04 eV. The effects of (harmonic) zero-point energy corrections to this difference are quite small (+0.002 eV for the neutral and −0.007 eV for the cation) as can be seen from Table IV.

Experimental confirmation of the cluster formation, albeit in its excited state, is given from the Xe$^+$ images at the various REMPI transitions around 363.9 nm. The VUV light produced at this wavelength is very close to the energy of the $5d[5/2]$, $J = 3$ level of atomic Xe at 82 430 cm^{-1}, but the one-photon transition to this state is of course forbidden ($\Delta J = \pm 1$). If the Xe$^+$ observed in the mass spectrum is produced from REMPI of atomic Xe, carrier gas, no Xe$^+$ recoil is anticipated and the image is expected to consist of a single

TABLE II. Energies (in a.u.) of Xe, Xe$^+$, Py, Py$^+$, and the two minima for (Xe–Py) and (Xe–Py)$^+$ at the MP2 level of theory with the basis sets of double through the quadruple zeta quality.

Species	Isomer	aug-cc-pVDZ/ aug-cc-pVDZ-PP	aug-cc-pVTZ/ aug-cc-pVTZ-PP	aug-cc-pVQZ/ aug-cc-pVQZ-PP
Xe		−328.425 045 4	−328.549 112 6	−328.661 616 8
Xe$^+$		−327.973 015 0	−328.093 650 5	−328.201 346 4
(Py)		−209.563 020 1	−209.748 373 4	−209.807 809 4
(Py)$^+$		−209.258 193 9	−209.437 916 7	−209.495 551 8
(Xe–Py)	m_1 (π bonded)	−537.993 644 9	−538.304 557 7	−538.477 554 6
	m_2 (H bonded)	−537.992 016 1	−538.302 396 1	−538.475 141 7
(Xe–Py)$^+$	m_1 (π bonded)	−537.689 850 5	−537.995 042 2	−538.166 078 4
	m_2 (H bonded)	−537.691 249 0	−537.996 997 6	−538.167 754 7

TABLE III. Harmonic vibrational frequencies (in cm^{-1}) for Py, Py$^+$, (Xe–Py), and (Xe–Py)$^+$ at the MP2//aug-cc-pVDZ/aug-cc-pVDZ-PP level of theory.

	(Xe–Py)			(Xe–Py)$^+$	
(Py) $X\,^1A_1\,(C_{2v})$	m_1 (π bonded) $^1A'\,(C_s)$	m_2 (H bonded) $^1A'\,(C_s)$	(Py)$^+$ $X\,^2A_2\,(C_{2v})$	m_1 (π bonded) $^2A\,(C_1)$	m_2 (H bonded) $^2A_2\,(C_{2v})$
515 (b_1)	50 (a')	40 (a'')	489 (b_1)	26	22 (b_2)
609 (a_2)	65 (a'')	45 (a')	499 (a_2)	49	61 (b_1)
637 (b_1)	66 (a')	53 (a')	687 (b_1)	67	71 (a_1)
665 (a_2)	515 (a')	526 (a'')	741 (b_1)	488	495 (b_1)
719 (b_1)	592 (a'')	610 (a'')	862 (a_2)	492	501 (a_2)
792 (b_1)	631 (a')	643 (a'')	869 (b_2)	680	739 (b_1)
817 (a_2)	659 (a'')	665 (a'')	883 (a_1)	737	768 (b_1)
859 (b_2)	715 (a')	719 (a'')	890 (b_1)	846	864 (a_2)
882 (a_1)	784 (a')	794 (a'')	914 (a_2)	869	872 (b_2)
107 (a_1)	801 (a'')	817 (a'')	1013 (b_2)	882	882 (a_1)
1056 (b_2)	858 (a'')	859 (a')	1080 (a_1)	884	899 (b_1)
1096 (a_1)	882 (a')	883 (a')	1114 (a_1)	901	912 (a_2)
1157 (b_2)	1036 (a')	1036 (a')	1181 (a_1)	1014	1016 (b_2)
1168 (a_1)	1055 (a'')	1056 (a')	1215 (b_2)	1080	1080 (a_1)
1292 (b_2)	1096 (a')	1096 (a')	1308 (b_2)	1114	1113 (a_1)
1431 (a_1)	1158 (a'')	1156 (a')	1493 (b_2)	1182	1184 (a_1)
1481 (b_2)	1168 (a')	1168 (a')	1518 (a_1)	1214	1219 (b_2)
1495 (a_1)	1291 (a'')	1290 (a')	1561 (a_1)	1307	1310 (b_2)
1545 (b_2)	1431 (a')	1431 (a')	3270 (b_2)	1493	1502 (b_2)
3272 (b_2)	1482 (a'')	1480 (a')	3293 (a_1)	1519	1518 (a_1)
3283 (a_1)	1495 (a')	1494 (a')	3294 (b_2)	1560	1562 (a_1)
3299 (b_2)	1544 (a'')	1543 (a')	3310 (a_1)	3277	3280 (b_2)
3305 (a_1)	3271 (a'')	3271 (a')	3479 (b_2)	3294	3294 (a_1)
3673 (a_1)	3283 (a')	3284 (a')	3609 (a_1)	3297	3296 (b_2)
	3297 (a'')	3300 (a')		3310	3310 (a_1)
	3304 (a')	3307 (a')		3577	3499 (a_1)
	3669 (a')	3671 (a')		3611	3703 (b_2)

TABLE IV. Calculated and experimentally determined energetics (in eV) of Xe, (Py), and the (Xe–Py) cluster and energy separation between the m_1 and m_2 minima. Numbers in parentheses include (harmonic) zero-point energy corrections.

| Energetics	aug-cc-pVDZ/ aug-cc-pVDZ-PP	aug-cc-pVTZ/ aug-cc-pVTZ-PP	aug-cc-pVQZ/ aug-cc-pVQZ-PP	Expt.
IP(Xe)	12.30	12.39	12.52	12.13[a]
IP(Py)	8.29 (8.44)	8.45 (8.59)	8.50 (8.64)	8.2
VIE(Xe–Py) wrt Xe+(Py)$^+$	8.40	8.57		
VIE(Xe–Py) wrt (Xe)$^+$+Py	12.41	12.51		12.05[b]
$\Delta E_{m_2-m_1}$, (Xe–Pyr)	0.044 (0.046)	0.059 (0.061)	0.066 (0.068)	
$\Delta E_{m_2-m_1}$, (Xe–Pyr)$^+$	−0.038 (−0.031)	−0.053 (−0.046)	−0.046 (−0.038)	
D_e(Xe–Py)$^+$, m_1	0.18	0.22	0.24	
D_0(Xe–Py)$^+$, m_1	0.16	0.20	0.23	
D_e(Xe–Py)$^+$, m_2	0.22	0.27	0.29	
D_0(Xe–Py)$^+$, m_2	0.19	0.25	0.26	
D_e(Xe–Py), m_1	0.15	0.19	0.22	
D_0(Xe–Py), m_1	0.16	0.20	0.23	
D_e(Xe–Py), m_2	0.11	0.13	0.16	
D_0(Xe–Py), m_2	0.11	0.14	0.16	

[a]Reference 26.
[b]This work.

TABLE V. Photoelectron peak energies and corresponding Xe$^+$ KER (see text for details).

Peak	e^- KER (eV)	Vertical energy (eV)	Xe$^+$ KER (eV)
A	1.28	12.35	0.073
B	1.17	12.46	0.11
C	1.08	12.55	0.14
D	0.95	12.68	0.19

spot. Clearly the appearance of the images and the deduced from of the KER spectrum in Fig. 9, suggests that the Xe$^+$ is produced from a molecular precursor.

The appearance of the photoelectron spectrum in Fig. 10 further confirms the presence of the (Xe–Py) cluster. The electron KER of the peaks in the spectrum is listed in Table V. Peak O in Fig. 10 is the band origin and to a first approximation we can assign it to the transition $[(Xe-Py), v''=0] \rightarrow [(Xe-Py)^+, v'=0]$. The total photon energy VUV+UV is 13.63 eV (10.22+3.41 eV). From the energy of peak O we determine that the vertical ionization energy (assuming that the electron is being removed from the Xe atom) for forming this particular state of the (Xe–Py)$^+$ cluster is 12.05±0.05 eV. We observe that this energy is 0.080 eV lower than the first ionization energy of Xe. The rest of the peaks correspond to overtones, i.e., $[(Xe-Py), v''=0] \rightarrow [(Xe-Py)^+, v'>0]$. It is also interesting that although the photoelectron spectrum appears fairly simple, only Xe$^+$ is observed in the mass spectrum and no (Xe–Py)$^+$ parent ion. This suggests that the parent ion must readily dissociate according to

$$(Xe - Py)^+ \rightarrow Xe^+(^2P_{3/2}) + (Py). \tag{1}$$
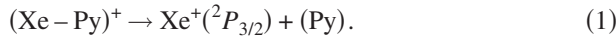
To determine the nature of the pyrrole fragment electronic state we consider a qualitative energy level diagram shown in Fig. 12. We notice that the energy of the asymptotic limit for forming Xe$^+(^2P_{3/2})$ and pyrrole ($X\,^1A_1$) in its ground electronic state (12.13 eV) is just below the channel forming neutral Xe($^1S_0$) and electronically excited pyrrole cation Py$^+(^2B_1)$ (formed by removing an electron from the $9a_1$ molecular orbital) located at approximately 13.0 eV. So

we assume that any (Xe–Py)$^+$ states formed from the photoionization process that lie above the energetic limit of 12.13 eV will *predissociate* into this channel. From the photoelectron KERs we can determine the excess energy E_a and subsequently the KER for the Xe$^+$ fragments via the relationship

$$KER(Xe^+) = \frac{m(Py)}{m(Py) + m(Xe)} E_a \tag{2}$$

The determined KER(Xe$^+$) values are listed in Table V and are plotted in Fig. 10(a). The agreement with the low energy structure in the KER spectrum obtained from the photofragment images is excellent. For the minor peaks F and D we perform the reverse calculation and from the measured Xe$^+$ KER we deduce that the corresponding e^- KER would be in the photoelectron spectrum and we plot the results in Fig. 10(b). These energies lie well within the photoelectron spectrum measured and are hence consistent with our model. Distinct features for these two minor channels are not resolved because of insufficient experimental sensitivity and signal to noise ratio.

Further support from the predissociation model suggested comes from the angular distribution of the Xe$^+$ photofragments at low energy, that are essentially isotropic, as expected for a relatively slow (with respect to the rotational period) predissociation process. On the other hand, peak X in Xe$^+$ KER in Fig. 10(a) is very anisotropic leading us to believe that this channel results from a direct photodissociation mechanism. This most probably involves the absorption of another UV photon that excites the ground state (Xe–Py)$^+$ cluster onto a dissociative state. We assume that this electronically excited cluster state also correlates asymptotically to the formation of Xe$^+(^2P_{3/2})$ and pyrrole ($X\,^1A_1$) and a qualitative diagram is shown in Fig. 13. Using conservation of energy and Eq. (2) we obtain

$$3.41\ eV - D_o[Xe \cdot Py]^+ = E_a$$

$$= KER(Xe^+)\frac{m(Py) + m(Xe)}{m(Py)}, \tag{3}$$

hence
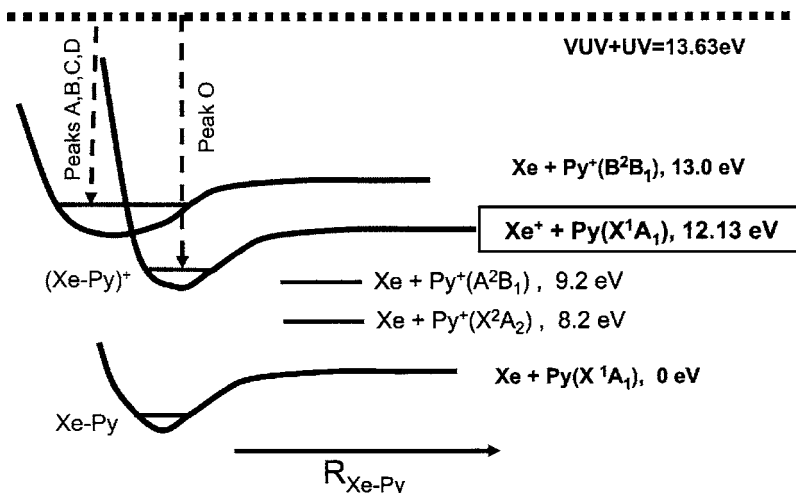
FIG. 12. Qualitative potential energy diagram for the dissociative photoionization of Xe–Py cluster.

Figure labels:
VUV+UV=13.63eV
Peaks A,B,C,D
Peak O
Xe + Py$^+$(B^{2}B$_1$), 13.0 eV
Xe$^+$ + Py(X^{1}A$_1$), 12.13 eV
Xe + Py$^+$(A^{2}B$_1$), 9.2 eV
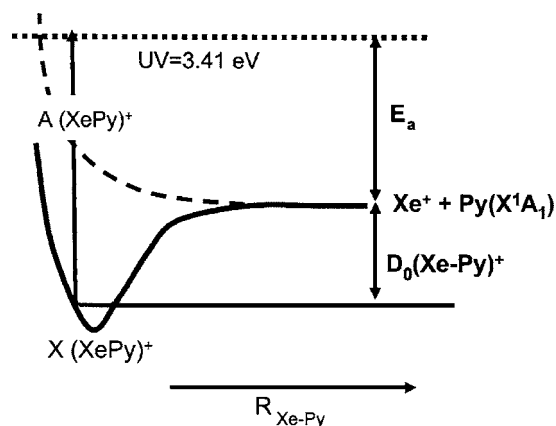Xe + Py$^+$(X^{2}A$_2$), 8.2 eV
Xe + Py(X ^{1}A$_1$), 0 eV
(Xe-Py)$^+$
Xe-Py
R_{Xe-Py}

FIG. 13. Qualitative potential energy diagram for the photodissociation of ground state $(Xe–Py)^+$ cluster.

$$D_o[Xe \cdot Py]^+ \sim 0.45 \pm 0.05 \text{ eV},$$

where the error bars are estimated from the average half-width of the peaks in the KER spectrum. The above value for $D_0(Xe–Py)^+$ for the excited state correlating with the $Xe^+ + Py(X^1A_1)$ asymptote (see Fig. 12) is an *upper limit* as we have assumed that all of the excess energy goes into product translational energy. This estimate for the binding energy of the excited state is not to be confused with our calculated value of similar magnitude for the ground state $D_0(Xe–Py)^+$ correlating with the $Xe+Py^+(X^2A_2)$ asymptote, listed in Table IV for the two minima of this cluster. The energetics of the excited states of the $(Xe–Py)^+$ cluster will be examined in a subsequent publication.

Using conservation of energy, the position of the origin of the photoelectron spectrum at 1.58 eV and the energy level diagram in Fig. 12 we write,

$$13.63 \text{ eV} = D_o[Xe \cdot Py] + 12.13 \text{ eV} - D_o[Xe \cdot Py]^+$$
$$+ 1.58 \text{ eV}, \qquad (4)$$

hence

$$D_o[Xe \cdot Py]^+ - D_o[Xe \cdot Py] \sim 0.08 \pm 0.05 \text{ eV}.$$

This corresponds to the difference in the binding energies between the ground state of the neutral (Xe–Py) and the excited state of the cation $(Xe–Py)^+$ cluster that correlates with the asymptote $Xe^++Py(X^1A_1)$, see Fig. 12. This energy difference should not be confused with the calculated (in Table IV) energy difference between the ground states of the neutral (Xe–Py) and the cation $(Xe–Py)^+$ cluster, the latter correlating with the $Xe+Py^+(X^2A_2)$ asymptote. As noted earlier the energetics of the excited states of the $(Xe–Py)^+$ cluster will be presented in a subsequent publication.

V. CONCLUSIONS AND OUTLOOK

Experimentally, we have demonstrated that when imaging H-atom photofragments, the $(1+1')$ REMPI scheme used in this work offers much higher resolution than the traditional $(2+1)$ REMPI at 243 nm. Concerning the UV photolysis of pyrrole we have confirmed the previous results of Ashfold and co-workers, namely, that in this region the

absorption is *selectively* induced by populating one or more quanta of vibration in the non-symmetric skeletal modes of the parent molecule. We have also spectroscopically identified the formation of the Xe–Py cluster when using Xe as the carrier gas in our molecular beam. The structure and dynamics of this cluster were discussed based both on the experimental and computational results presented.

A question, which still remains unanswered, is why the cluster formation apparently quenches N–H bond fission. Cluster formation generally tends to shift valence absorption bands to the red and, consequently, it is not obvious that the closing of the H-atom fragment channel should occur for energetic reasons, i.e., shifting of the energetic threshold.

Though in the present study we have spectroscopically identified only the Xe–Py cluster, the presence of higher order clusters $Xe–Py_N$ ($N=1,2,3,\dots$) cannot be ruled out. However, our low stagnation pressures and relatively large nozzle diameter lead us to doubt whether Xe "snowball" effects, i.e., entrainment of pyrrole molecules in large Xe clusters, could provide an explanation.

In the case of the dimer cluster, does the presence of the heavy Xe atom inhibit the nontotally symmetric skeletal vibrations that, considering the conclusions of Ashfold and co-workers, promote the fast H-atom release, therefore shutting down the N–H bond fission channel? Our current results (see Table III) suggest that the vibrational spectrum of (Py) is only weakly perturbed by the presence of one Xe atom. So this drastic effect should not be attributed to changes in the vibrational degrees of freedom. Additional electronic structure calculations aiming to understand how the presence of the noble gas affects the excited state manifold of pyrrole in order to address this question are currently under way.

[1] A. L. Sobolewski and W. Domcke, Chem. Phys. Lett. **315**, 293 (1999).
[2] A. L. Sobolewski and W. Domcke, Chem. Phys. **259**, 181 (2000).
[3] A. L. Sobolewski and W. Domcke, J. Phys. Chem. A **105**, 9275 (2001).
[4] A. L. Sobolewski, W. Domcke, C. Dedonder-Lardeux, and C. Jouvet, Phys. Chem. Chem. Phys. **4**, 1093 (2002).
[5] Y. Okumura, Y. Sugiyama, and K. Okazaki, Fuel **81**, 2317 (2002) and references therein.
[6] R. A. Jones, E. C. Taylor, and A. Weissberger, *Pyrrole: The Chemistry of Heterocyclic Compounds* (Wiley, New York, 1990).
[7] P. A. Mullen and M. K. Orloff, J. Chem. Phys. **51**, 2276 (1969).
[8] M. Bavia, F. Bertinelli, C. Taliani, and C. Zauli, Mol. Phys. **31**, 419 (1976).

[9] M. H. Palmer, I. C. Walker, and M. F. Guest, Chem. Phys. **238**, 179 (1998).

[10] B. O. Roos, P. A. Malmqvist, V. Molina, L. Serrano-Andres, and M. Merchan, J. Chem. Phys. **116**, 7526 (2002).

[11] J. Wan, J. Meller, M. Hada, M. Ehara, and H. Nakatsujia, J. Chem. Phys. **113**, 7853 (2002).

[12] D. A. Blank, S. W. North, and Y. T. Lee, Chem. Phys. **35**, 187 (1994).

[13] J. Wei, A. Kuezmann, J. Riedel, F. Renth, and F. Temps, Phys. Chem. Chem. Phys. **5**, 315 (2003); J. Wei, J. Riedel, A. Kuczmann, F. Renth, and F. Temps, Faraday Discuss. **127**, 267 (2004).

[14] B. Cronin, M. G. D. Nix, R. H. Qadiri, and M. N. R. Ashfold, Phys. Chem. Chem. Phys. **6**, 5031 (2004).

[15] L. Serrano-Andres, M. Merchan, I. Nebot-Gil, B. O. Roos, and M. Fulscher, J. Am. Chem. Soc. **115**, 6184 (1993).

[16] C. R. Gebhardt, T. P. Rakitzis, P. C. Samartzis, V. Ladopoulos, and T. N. Kitsopoulos, Rev. Sci. Instrum. **72**, 3848 (2001).

[17] V. Papadakis and T. N. Kitsopoulos, Rev. Sci. Instrum. **77**, 083101 (2006).

[18] D. Proch and T. Trickl, Rev. Sci. Instrum. **60**, 713 (1989).

[19] C. Møller and M. S. Plesset, Phys. Rev. **46**, 618 (1934).

[20] T. H. Dunning, Jr., J. Chem. Phys. **90**, 1007 (1989); R. A. Kendall, T. H. Dunning, Jr., and R. J. Harrison, *ibid.* **96**, 6796 (1992).

[21] K. A. Peterson, D. Figgen, E. Goll, H. Stoll, and M. Dolg, J. Chem. Phys. **119**, 11113 (2003).

[22] M. J. Frisch, G. W. Trucks, H. B. Schlegel, GAUSSIAN 03, Revision C.02, Gaussian, Inc., Wallingford, CT, 2004.

[23] L. Schnieder, W. Meier, K. H. Welge, M. N. R. Ashfold, and C. M. Western, J. Chem. Phys. **92**, 7027 (1990).

[24] R. L. Toomes, P. C. Samartzis, T. P. Rakitzis, and T. N. Kitsopoulos, Chem. Phys. **301**, 209 (2004).

[25] M. N. R. Ashfold, B. Cronin, A. L. Devine, R. N. Dixon, and M. G. D. Nix, Science **312**, 1637 (2006).

[26] *CRC Handbook of Chemistry and Physics*, edited by D. R. Lide (CRC, Boca Raton, FL, 1992), pp. 10–21; C. E. Moore, *Ionization Potentials and Ionization Limits Derived from the Analyses of Optical Spectra*, Natl. Stand. Ref. Data Ser. (U.S. GPO, Washington, D.C., 1970), Vol. 34.